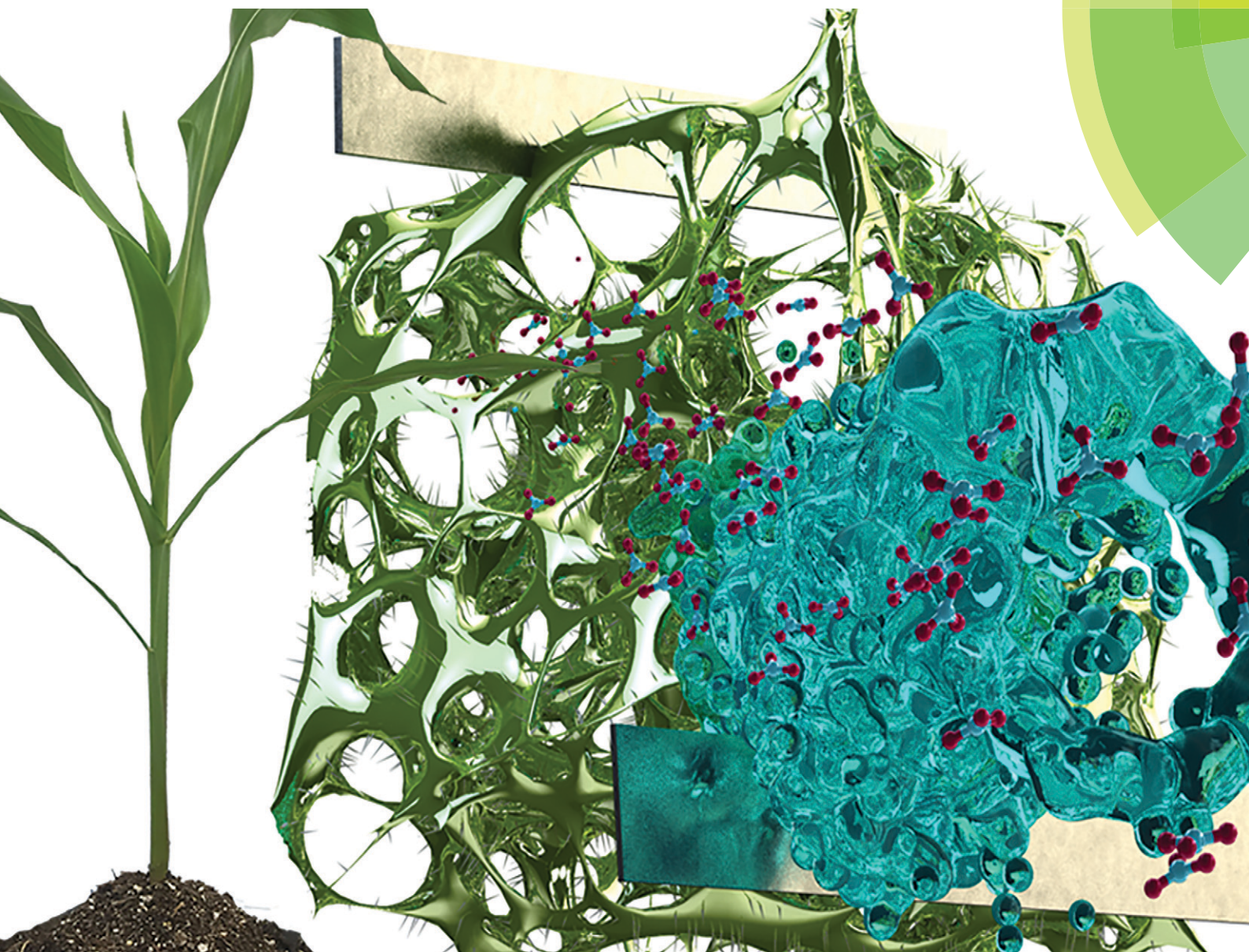# Lab on a Chip

Miniaturisation for chemistry, physics, biology, materials science and bioengineering

rsc.li/loc

ROYAL SOCIETY OF CHEMISTRY

PAPER
Liang Dong *et al.*
In situ integration of graphene foam–titanium nitride based bio-scaffolds and microfluidic structures for soil nutrient sensors

CrossMark
click for updates

In situ integration of graphene foam–titanium nitride based bio-scaffolds and microfluidic structures for soil nutrient sensors†

Md. Azahar Ali,[a] Kunal Mondal,[b] Yifei Wang,[a] Huawei Jiang,[a] Navreet K. Mahal,[c] Michael J. Castellano,[c] Ashutosh Sharma[d] and Liang Dong*[a]

It is challenging to integrate porous graphene foam (GF) and GF-based nanocomposites into microfluidic channels and even create microfluidic structures within these materials. This is because their irregular interior pore shape and geometry, rough exterior surface, and relatively large material thickness make it difficult to perform conventional photolithography and etching. This challenge has largely hindered the potential of using GF-based materials in microfluidics-based sensors. Here we present a simple approach to create well-defined flow-through channels within or across the GF-based materials, using a liquid-phase photo-polymerization method. This method allows embedding of a nanocomposite-based scaffold of GF and titanium nitride nanofibers (GF–TiN NFs) into a channel structure, to realize flow-through microfluidic electrochemical sensors for detecting nitrate ions in agricultural soils. The unique GF–TiN nanocomposite provides high electrochemical reactivity, high electron transfer rate, improved loading capacity of receptor biomolecules, and large surface area, serving as an efficient electrochemical sensing interface with the help of immobilized specific enzyme molecules. The microfluidic sensor provides an ultralow limit of detection of 0.01 mg L^{-1}, a wide dynamic range from 0.01 to 442 mg L^{-1}, and a high sensitivity of 683.3 µA mg^{-1} L cm^{-2} for nitrate ions in real soil solution samples. The advantageous features of the GF–TiN nano-composite, in conjunction with the *in situ* integration approach, will enable a promising microfluidic sensor platform to monitor soil ions for nutrient management towards sustainable agriculture.

Introduction

Microfluidic sensors provide many benefits such as high portability, low consumption of agents and reagents, high sensitivity, fast response, and process parallelization.[1,2] Integration of nanostructured functional materials into microfluidic sensors has demonstrated a potential to enhance biological and chemical sensing capabilities.[3,4] For example, carbon nanotubes (CNTs) and zinc oxide nanowires were integrated into microfluidic electrochemical sensors for the detection of dopamine, catechol,[4] and environmental pH conditions[3] with improved sensitivity and stability, owing to an increased sensing surface area and electrochemical reactivity. A high-performance sensing interface was also established by integrating polyaniline–CNTs into microfluidic channels to quantify physiochemical glucose and pH in biological tissues.[5] In addition, introduction of nickel oxide nanowires into microfluidic sensors led to an enhanced loading capacity of receptor biomolecules and thus an improved sensitivity.[6]

Notably, as an interconnected three-dimensional (3D) network of graphene, graphene foam (GF) has recently been realized by chemical vapor deposition of graphene on a metal foam based template[7] and has demonstrated to provide a powerful platform for biochemical sensing,[8] water remediation,[9] and energy storage.[10] In particular, the networked interior surfaces of GF provide a suitable environment to attract functional nanomaterials *via* electrostatic interactions.[11] Consequently, several GF-based composites have been developed as electrochemical electrode materials[11,12] *via* nitrogen doping[13] and surface functionalization with various metal oxides (*e.g.*, cobalt oxide,[11] copper oxide,[14] manganese oxide,[12] titanium oxide,[15] and silver nanowires).[16] It is believed that the composites of GF and nanomaterials are strong candidates

a Department of Electrical and Computer Engineering, Iowa State University, Ames, Iowa 50011, USA. E-mail: ldong@iastate.edu; Tel: +1 515 294 0388
b Department of Chemical and Biomolecular Engineering, North Carolina State University, Raleigh, North Carolina 27695, USA
c Department of Agronomy, Iowa State University, Ames, Iowa 50011, USA
d Department of Chemical Engineering, Indian Institute of Technology Kanpur, Kanpur 208016, India

for new-generation microfluidics-based electrochemical sensors, owing to their fast transport of charge carriers, large surface area, high electrical conductivity and mechanical strength, and ease of functionalization with receptor biomolecules.[11–17] However, GF and GF-based composites appear porous with irregular pore shapes and rough external surfaces that are unfavorable for photolithography; in addition, they are relatively thick on the millimeter (mm) or sub-mm scale with networked scaffold structures[7,18] that are unfavorable for directional deep etching. Therefore, direct patterning of GF and GF-based composites or creation of microfluidic structures inside the materials is challenging to achieve by conventional photolithography and etching techniques. This has significantly limited their applications in microfluidic sensors and other devices. Recently, we have manually assembled a GF-based sensing material into a microfluidic immunosensor through hole drilling, material insertion, and epoxy glue application and curing.[15] The manual assembly process was relatively complex and had limited control over the position of the patterns. In addition, the assembled structure had relatively low robustness.

Functionalized nanofibers (NFs) can provide many excellent properties suitable for chemical and biological sensor applications,[19,20] including high aspect ratio, large surface area, and high electrochemical reactivity.[21] For example, NF-based titanium dioxide (TiO_2) have received increasing attention as an environmentally benign and structurally stable electrode material for the detection of relative humidity,[22] blood cholesterol,[23] and cancer biomarkers.[20] However, when functionalized with biomolecules, electrochemical conductivity of TiO_2 NFs significantly reduces, owing to the presence of oxygen vacancies and Ti–O bonds that restricts electron transfer.[23] To overcome this issue, researchers have recently developed nanostructured titanium nitride (TiN) by replacing the oxygen in TiO_2 with nitrogen[24–28] to achieve improved electrical conductivity, electron transport rate, and chemical stability. However, TiN NFs have little been explored in the area of electrochemical based biochemical sensors.

Here we report on an *in situ* integration method to seamlessly assemble a novel nanocomposite of GF–TiN NFs and a microfluidic channel together to realize a high-performance electrochemical soil nutrient sensor. A liquid-phase polymerization process[29,30] is employed to overcome the difficulty of assembling any GF or GF-based composites into microfluidic devices associated with the porous and irregular-shaped interior structure, poor surface morphology, and large thickness of these porous materials. We demonstrate the *in situ* formation of microfluidic channels within or across the GF–TiN scaffolds. This makes it convenient to realize a microfluidic sensor using the GF–TiN NFs as an electrochemical electrode material. In addition, from a material perspective, carbon doped TiN NFs are developed to modify the GF scaffolds; the combination of TiN NFs and GF generates a new hierarchical 3D composite electrode that has an improved electrochemical reactivity,

heterogeneous electron transfer rate, and loading capacity of receptor biomolecules specific to target analytes. Analyte solutions can flow through and strongly interact with receptor biomolecules immobilized at the surfaces of GF–TiN scaffolds for biochemical sensing.

While the GF–TiN NF composite can be tailored to detect a variety of biochemical molecules through appropriate surface functionalization, we present a microfluidic nitrate sensor (Fig. 1a and b) by immobilizing a nitrate reductase (NaR) enzyme onto the embedded GF–TiN NF composite to form NaR/GF–TiN NF based bio-scaffolds. This is owing to emerging global interest in sustainable agriculture and environment, where nitrogen (N) is one of the most important macronutrients for crop production in agriculture.[31,32] The precise and timely measurement of the availability of plant nutrients in soil can enable a precise nutrient application in farming. By monitoring soil nitrate dynamics,[31–37] farmers can optimize the N fertilizer inputs to enhance crop production. Managing nitrate input to agricultural soils can result in substantial economic return for farmers. Remarkably, our nitrate sensor has demonstrated an extremely low limit of detection (LOD) of 0.01 mg L^{-1} to accurately and rapidly detect nitrate concentrations in real samples extracted from agricultural soils. The high sensitivity of this sensor is ensured by an enhanced loading capacity of NaR enzyme molecules immobilized on the 3D matrix of the GF–TiN NF composite embedded in the microfluidic channel (Fig. 1c–f). The efficient surface functionalization allows sufficient conversion of nitrate to nitrite ions producing electrons.

Materials and methods

Chemicals

1.1 mm-thick GF with 99% carbon content (mutilayered; density: 4.0 mg cm^{-3}; mean pore size: 580 μm) was obtained from Graphene-Supermarket (Calverton, NY, USA). Titanium isopropoxide (Ti(OiPr)$_4$; molecular weight: 284.2 g mol^{-1}), PVP, N-hydroxysuccinimide (NHS), N-ethyl-N_0-(3-dimethylaminopropyl)carbodiimide (EDC), and lyophilized powder (≥300 units per g) of nitrate reductase (NAD[P]H) isolated from *Aspergillus niger* were obtained from Sigma-Aldrich (St. Louis, MO, USA). Potassium nitrate (KNO_3), potassium hydroxide (KOH), sodium chloride (NaCl), sodium bicarbonate ($NaHCO_3$), sodium sulfate ($Na_2SO_4·10H_2O$) and pyridine were obtained from Fisher Scientific (Hampton, NH, USA). Deionized (DI) water (resistivity: 18.2 MΩ cm) was homemade using a DI water generator (Millipore, Billerica, MA, USA). All chemicals utilized in this work were of analytical grade and used as obtained without any purification.

Synthesis of TiN NFs

To obtain TiN NFs, TiO_2 NFs were synthesized by an electrospinning technique using a Ti(OiPr)$_4$ precursor material.[23] In this step, PVP (0.9 g) was mixed with ethanol
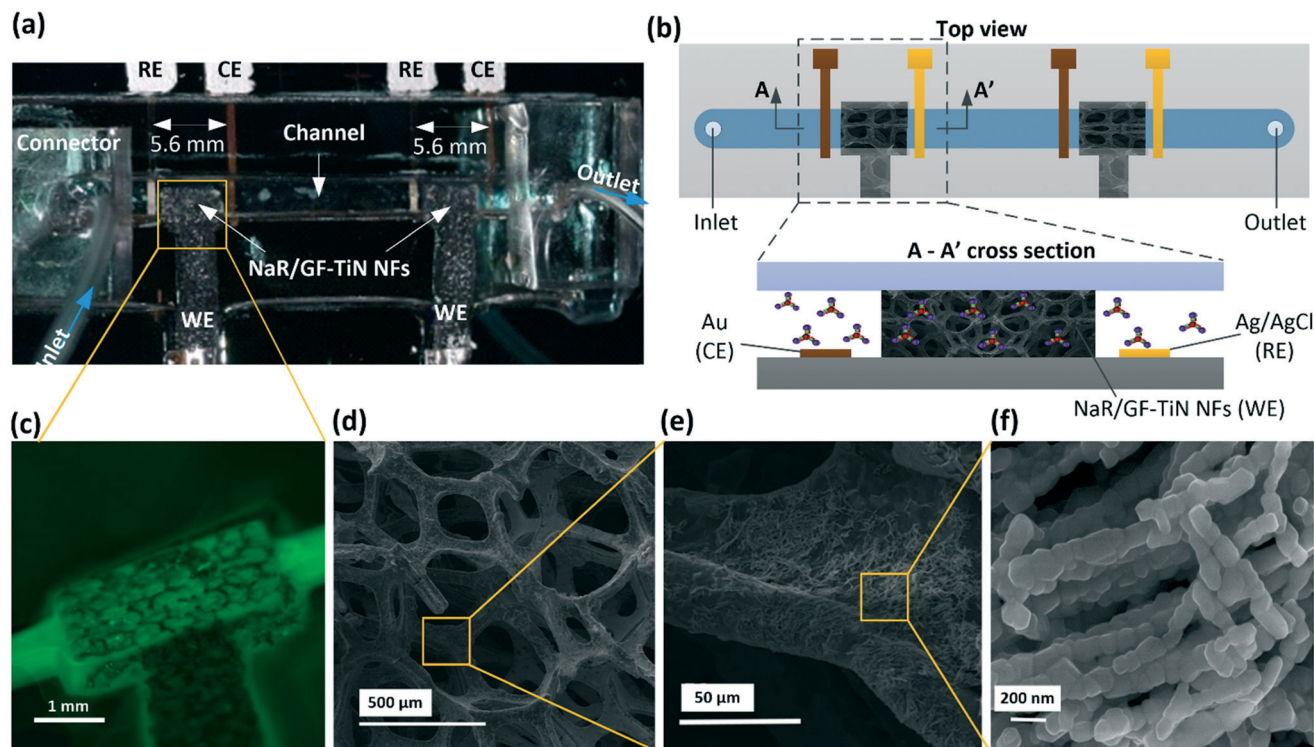
Fig. 1 (a) Photograph of a microfluidic device for detection of nitrate ions. Two sensors are formed in a channel. (b) Schematic representation of the sensor using embedded GO-TiN NFs as a working electrode. The GO-TiN NFs are functionalized with NaR enzyme molecules to realize specific detection of nitrate ions. Upper panel: schematic top view of the device. Lower panel: schematic cross-sectional view of the device at section A–A'. (c) Fluorescence image showing *in situ* integration of a GO–TiN NF based electrode into a channel using a liquid-phase photopolymerization process. The channel is built across the porous electrode. Field emission scanning electron microscopy (FESEM) images of the GF–TiN NF composite (d), details of the GF scaffolds modified by TiN NFs (e), and a close-up of TiN NFs (f).

solution (15 mL) and stirred for 5 min. Separately, Ti(OiPr)$_4$ (3.0 g) was added into a mixture of ethanol and acetic acid at a volume ratio of 1:1 and stirred thoroughly. Subsequently, the PVP solution was mixed with the Ti(OiPr)$_4$ solution. A 30 mL solution of the obtained electrospinning precursor solution was stirred for an hour and immediately loaded into a syringe having a stainless steel needle (26 gauges). A 15 kV high-voltage power supply (Gamma High Voltage, High Bridge, NJ, USA) was applied to the needle. The feed rate of the precursor solution was controlled using a syringe pump (Harvard Apparatus, Holliston, MA, USA). Electrospun TiO$_2$ NFs were collected with the help of a rotating drum wrapped with an aluminium foil and horizontally positioned at a 5 cm distance to the needle. The PVP/Ti(OiPr)$_4$ composite NFs were kept overnight in air and calcined at 400 °C for 2 h (2 °C min^{-1} ramp rate) in order to remove the polymer. After that, the as-synthesized TiO$_2$ NFs were subjected to heat treatment under an inert argon gas and ammonia atmosphere at 950 °C for 2 h. The carbonization occurred to the residual carbon from the unburned PVP polymer, and ammonia gas started the conversion of TiO$_2$ to the titanium oxynitride (TiO$_x$N$_y$) phase by doping N into the TiO$_2$ system.[25] Subsequently, the argon flow was removed and only NH$_3$ was exposed to 1050 °C, at which the TiO$_2$ NFs were completely converted into TiN

NFs. Also a small amount of carbon was present in TiN NFs which could bind with NaR enzyme molecules *via* covalent interactions. The synthesis steps for TiN NFs are schematically given in Fig. S1 (ESI†).

Sensor fabrication process

Fig. 2 shows the process flow for fabricating the microfluidic nitrate sensor. First, gold (Au, counter) and silver/silver chloride (Ag/AgCl, reference) electrodes are patterned on a silicon dioxide (SiO$_2$) layer grown on a silicon wafer. In this step, e-beam evaporation was used to deposit an 80 nm-thick Au layer on the Si/SiO$_2$ substrate and conventional photolithography was used to form the patterns of Au electrodes through a photomask printed on a transparency film (Fineline Imaging, Colorado Springs, CO, USA). Next, the Au layer was selectively etched using the Au etchant (GE-8148; Transene, Danvers, MA) to form counterelectrodes. Subsequently, similar procedures were adopted for the fabrication of Ag electrodes, where a 700 nm-thick Ag layer was selectively etched using the Ag etchant (Silver Etchant TFS; Transene, Danvers, MA). The Ag electrodes were treated with KCl (0.1 M) for 2 min to form the Ag/AgCl reference electrode. The gap between the Au and Ag/AgCl electrodes is 5.6 mm.
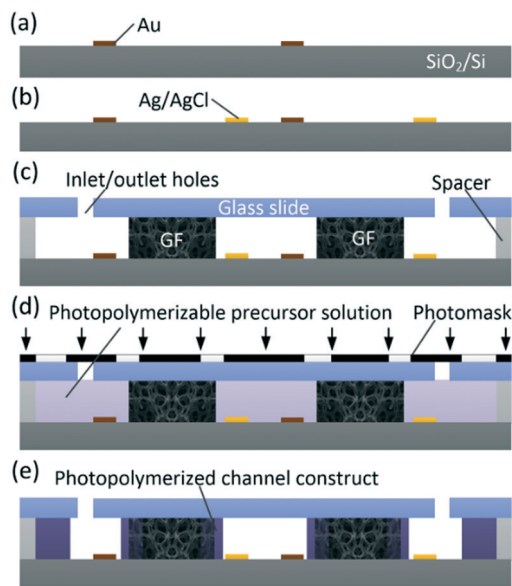
Fig. 2 Schematic representation of the main fabrication processes for the sensor. (a and b) Patterning of Au and Ag/Ag/Cl electrodes. (c) Formation of a cavity with GF–TiN NFs between a top glass slide and a silicon substrate. (d) *In situ* liquid-phase photopolymerization with a photomask and UV-sensitive precursor polymer solutions. (e) Formation of the channel and embedding of GF within the channel.

Second, a composite of GF–TiN NFs (4 mm × 2.4 mm × 1.1 mm) was formed. In this step, the synthesized TiN NFs were fragmented and dispersed in an ethanol solution (2 mg mL^{-1}) using a stirrer. The dispersion solution (50 μL) was drop coated at a pre-cut GF and then rested for 2 h to form a composite of GF–TiN NFs. The composite was washed with DI water and air-dried.

Third, a liquid-phase photopolymerization process was used to integrate the GF–TiN NF composite into a microfluidic channel on the substrate containing both the Au and Ag/AgCl electrodes. In this step, the composite was treated with oxygen plasma using a FEMTO Plasma Cleaner (power: 100 watts; time: 10 s; Diener Electronic, Ebhausen, Germany). Due to the large mean pore size (~580 μm) and high porosity (>90%) of GF, oxygen plasma could easily penetrate and modify the scaffolds of the composite. This would allow effective immobilization of nitrate reductase enzyme molecules on both the exterior and interior surfaces of the composite (the immobilization process will be described later). The oxygen plasma treated composite was then positioned between the Ag/AgCl and Au electrodes. Following that, 1.1 mm-thick polydimethylsiloxane spacers (with the same thickness as that of the GF–TiN NF composite) were emplaced between the device substrate and a 1 mm-thick top glass slide to form an air cavity. The top glass slide was pre-punched to form two through-holes as an inlet and an inlet of a channel using a conventional milling machine with a 1 mm-diameter diamond drill bit. Separately, a photopatternable precursor solution was prepared by mixing a monomer, isobornyl acrylate (IBA), a crosslinker, tetraethylene glycol dimethacrylate

(TeGDMA), and a photoinitiator, 2,2-dimethoxy-2-phenylacetophenone (DMPA), at a weight ratio of 31.66 : 1.66 : 1.0.[29,30,38] The precursor solution was injected into the cavity using a conventional plastic pipette. Note that the precursor solution could easily penetrate the interior of the GF–TiN composite to fill the whole cavity. After that, a transparency film based photomask (Fineline Imaging, Colorado Springs, CO, USA) was placed on top of the glass slide. The device was exposed under ultraviolet (UV) light (intensity: 12 mW cm^{-2}) for 95 s through the photomask. The UV exposed solution was polymerized. The channel was formed by rinsing the device with ethanol (Sigma-Aldrich, St. Louis, MO, USA) for 5 min to remove the unpolymerized precursor solution. The device was baked on a hotplate at 60 °C for 1 h to remove solvents. Therefore, the *in situ* assembly of the GF–TiN NFs into the microfluidic channel was realized.

Finally, the embedded GF–TiN NF composite was functionalized with NaR enzyme molecules. In this step, the NaR solution (3.5 mg mL^{-1}) was mixed with a 50 μL EDC–NHS solution (EDC: 0.2 M; NHS: 0.05 M; mixing volume ratio of 1 : 1) and then injected into the channel of the device.[44,48] After that, the device was kept in a humid chamber for 4 h at 23 °C and another 12 h at 4 °C. Here, the water-soluble EDC reacted with carboxylic acid groups present in the GF–TiN NF composite to form an intermediate *O*-acylisourea which was unstable in aqueous solutions (Fig. S2 in the ESI†), while the NHS solution improved the efficiency of covalent interactions by creating an intermediate amine-reactive NHS ester. The NHS ester was more stable compared to *O*-acylisourea, allowing for efficient conjugation with primary amines of NaR enzyme molecules *via* formation of covalent amide bonds (Fig. S2 in the ESI†). Lastly, a phosphate buffered saline (PBS) solution (pH 7.4) was used for removing any unbound enzyme molecules from the electrode surface. Therefore, the microfluidic sensor was formed.

Instrumentation

FESEM (Supra 400VP Gemini, Jena, Germany) and TEM (Tecnai™ G2, OR, USA) measurements were conducted to investigate the morphologies of the synthesized TiN NFs and GF–TiN NFs. XRD measurements were conducted to study nanocrystallization, nitrogen doping, and carbon traces in TiN NFs using the X'Pert PRO MRD system (PANalytical, Almelo, the Netherlands) with Cu Kα radiation (λ = 1.54 Å). Raman spectroscopy was performed using the WiTec alpha-300 system (WiTec, Ulm, Germany) with a 532 nm-wavelength laser. Further, Brunauer–Emmett–Teller (BET, Quantachrome Instruments, Florida, USA) measurements were conducted to investigate the specific surface area, average pore diameter and pore volume of TiN NFs. The formation of an amide bond between the enzyme and GF–TiN NFs was confirmed by XPS (Kratos Amicus/ESCA 3400 instrument, Manchester, UK). The samples exposed to 240 W unmonochromated Mg Kα X-rays and photoelectrons

emitted at 0° from the surface normal were analyzed using the DuPont analyzer. The pass energy level was set at 75 eV and the Shirley baseline was removed from all reported spectra. All electrochemical measurements were performed using an electrochemical workstation (DY2100; Digi-Ivy, TX, USA) in PBS solution (pH 7.4) containing an equimolar concentration (5 mM) for both $[Fe(CN)_6]^{3-}$ and $[Fe(CN)_6]^{4-}$ as redox mediators.

Synthetic and real sample preparation

To prepare synthetic test samples with different concentrations of nitrate ions, a stock solution of KNO_3 is prepared in PBS solution (pH 7.4). This solution is then diluted to several nitrate concentrations from 442 mg L^{-1} to 0.01 mg L^{-1} for electrochemical measurements. The preparation procedures and the concentration calibration of real samples extracted from agricultural soils are described in Fig. S3 (ESI†).

Results and discussion

In situ integration of microfluidic channels and GF-based materials

Fig. 3a shows the schematic of the liquid-phase photopolymerization process for integrating a channel and a GF–TiN NF based composite together. Microfluidic channels with
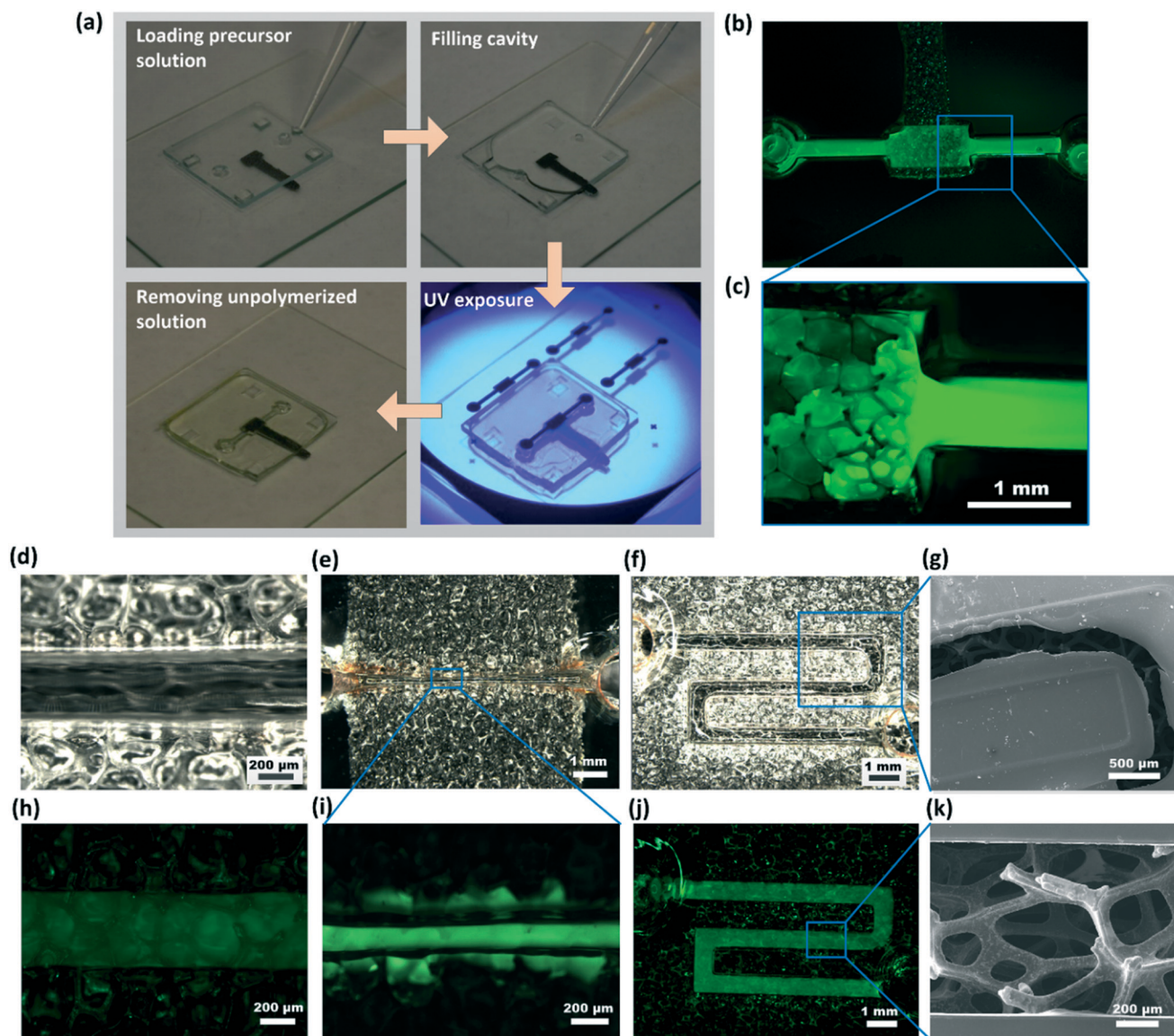
Fig. 3 (a) Schematic representation of the main steps for integrating GF–TiN and a microfluidic channel together. No Au or Ag/AgCl electrodes are made on the same substrate. (b) Fluorescence image showing a channel across an embedded GF–TiN electrode. (c) Close-up of the assembled structure in (b) showing the spatial transition from the non-GF to GF regions. (d–f) Optical images showing the microfluidic channels embedded within GF–TiN. (h–j) Fluorescence images corresponding to (d)–(f). (g and k) SEM images showing a close-up of the serpentine microfluidic channel in (f) and (j). The structure above the channel in (g) is opened for imaging the embedded GF–TiN.

various shapes and dimensions are created directly within or across the GF using different photomasks (Fig. 3b–k). Due to the networked and porous interior structures of the GF, the normal incident UV light may be reflected and scattered at the interior surfaces of the scaffolds on the light path. This allows photopolymerization of the filled precursor solution in the shadow of the scaffolds. The channels in Fig. 3d–k are well defined inside the GF, even though the channel width is less than the mean pore size of the GF ($\sim$580 μm). These formed "porous" channels allow liquids to flow through along a defined flow path. It should be noted that the edges of the embedded channels are a little jagged because of the light scattering during the photopolymerization process, as shown in a close-up of the embedded 200 μm-wide microfluidic channel (Fig. 3i).

Because the photosensitive precursor solution has low viscosity and high transparency, it can easily fill in the irregular-shaped interior structures of porous materials during the liquid-phase photopolymerization process.[29,30,38] Generally, the liquid-phase photopolymerization method requires a polymer precursor solution, consisting of a monomer, a cross-linker, and a photoinitiator, for forming microfluidic channels. Besides the mixture of IBA, TeGDMA, and DMPA utilized here, many other precursor solutions can be employed to create channels inside GF-based materials using the same method, such as a prepolymer mixture of 2-hydroxyethylmethacrylate (monomer), ethylene glycol dimethacrylate (cross-linker), 2,2-dimethoxy-2-phenylacetophenone (photo-initiator) and water[39] and another mixture of IBA, TeGDMA, and Irgacure 651.[29] Due to the fluid nature and high porosity of the GF-based materials, the unpolymerized precursor solution can be easily removed by flushing the channel with water or ethanol, provided that the channel is high enough not to be blocked by individual scaffolding materials (note: 100–150 μm-thick nickel was used as the base scaffolding material of GF). In addition, due to the light scattering at the GF scaffold, overcut patterns of the channels were observed and the minimum channel width was found to be 200 $\pm$ 120 μm, as shown in Fig. 3i. The spatial resolution of the channels may be improved by fine-tuning the photopolymerization conditions and optimizing the shapes and dimensions of the scaffolding materials to minimize the light scattering effect. In addition, it is worthwhile to point out that this integration method does not utilize any spinning or casting of photosensitive materials, wherein self-planarization of the rough external surfaces of the GF can be achieved. The whole process of integrating channels and GF and GF-based composites requires only about a couple of minutes, eliminating complex and inaccurate manual assembly steps.

Characterization of the GF–TiN NF based composite

The synthesis of TiN NFs involves the formation of TiO_2 NFs using an electrospinning technique and subsequent replacement of the oxygen in TiO_2 NFs with nitrogen under an argon and ammonia gas atmosphere at a high temperature.[25] Detailed descriptions of the material synthesis are described in the materials and methods section.

First, X-ray diffraction (XRD) is conducted to investigate the nanocrystallinity of TiN NFs converted from TiO_2 NFs. The XRD pattern in Fig. S4a (ESI†) demonstrates the formation of major crystallographic planes associated with the cubic crystal structure of anatase TiN,[40] along with other planes for Ti_2N, TiON and rutile TiO_2. A small amount of residual carbon is found remaining in TiN NFs. This is because of the incomplete removal of the carrier polymer polyvinylpyrrolidone (PVP) during calcination which later is converted to carbon during the heat treatment (as described in the materials and methods section). In addition, Raman spectroscopy studies in Fig. S4b (ESI†) also show that TiN NFs have mixed rutile and anatase phases[41] where the well-defined disorder (D) and graphitic (G) bands exist due to the formation of amorphous carbon in TiN NFs. More detailed explanations of the results from XRD and Raman measurements are described in the ESI.†

Next, X-ray spectroscopy (XPS) studies are performed to investigate the nitrogen doping and carbon contents in TiN NFs alone (without GF) and to confirm the immobilization of NaR enzyme molecules on the surface of the GF–TiN NF composite. The $2p_{1/2}$ peak at 463.8 eV in the XPS spectra (Fig. S5, ESI†) are ascribed to Ti–O bonds. The nitrogen doping to TiO_2 NFs causes the binding energy of the $2p_{1/2}$ peak to shift to 3.9 eV, due to the formation of Ti–N bonds. The N1s spectra shown in Fig. S6a (ESI†) further demonstrate successful nitrogen doping and a trace amount of C–OH groups in TiN NFs.[28]

Fig. 4 shows the deconvolution peaks of C1s and N1s for GF–TiN NF and NaR/GF–TiN NF electrodes, respectively. The XPS peaks at binding energies of 284.0 eV and 284.9 eV in GF–TiN NFs correspond to the core level of carbon, due to sp^2-carbon (non-oxygenated C in the C–C bond) and sp^3-carbon (oxygenated C in the C–O bond), respectively (Fig. 4a). Two additional peaks at 285.4 eV and 298.1 eV in GF–TiN NFs are assigned to C=O and carboxylic groups (O–C=O), respectively, arising due to the oxygen plasma treatment to the GF–TiN NF composite before NaR immobilization. The presence of O–C=O groups in GF–TiN NFs can facilitate binding with NH_2 groups in NaR via covalent amide (C–N) bonds. The in situ immobilization of NaR on the scaffolds of GF–TiN NFs results in an additional peak at 287 eV, due to the formation of N–C=O bonds between the NaR and GF–TiN NFs. The N 1s core-level spectra of GF–TiN NFs before and after the NaR immobilization confirm the presence of nitrogen atoms (Fig. 4b). After the NaR immobilization, two peaks appear at 399.9 eV and 400.8 eV, which are assigned to the core-level spectra of N 1s (–N=) and the amide bond (C=O–NH) between NaR and GF–TiN NFs, respectively. Therefore, the in situ NaR immobilization is confirmed by the observed strong covalent bond (i.e., C–N) on the bio-
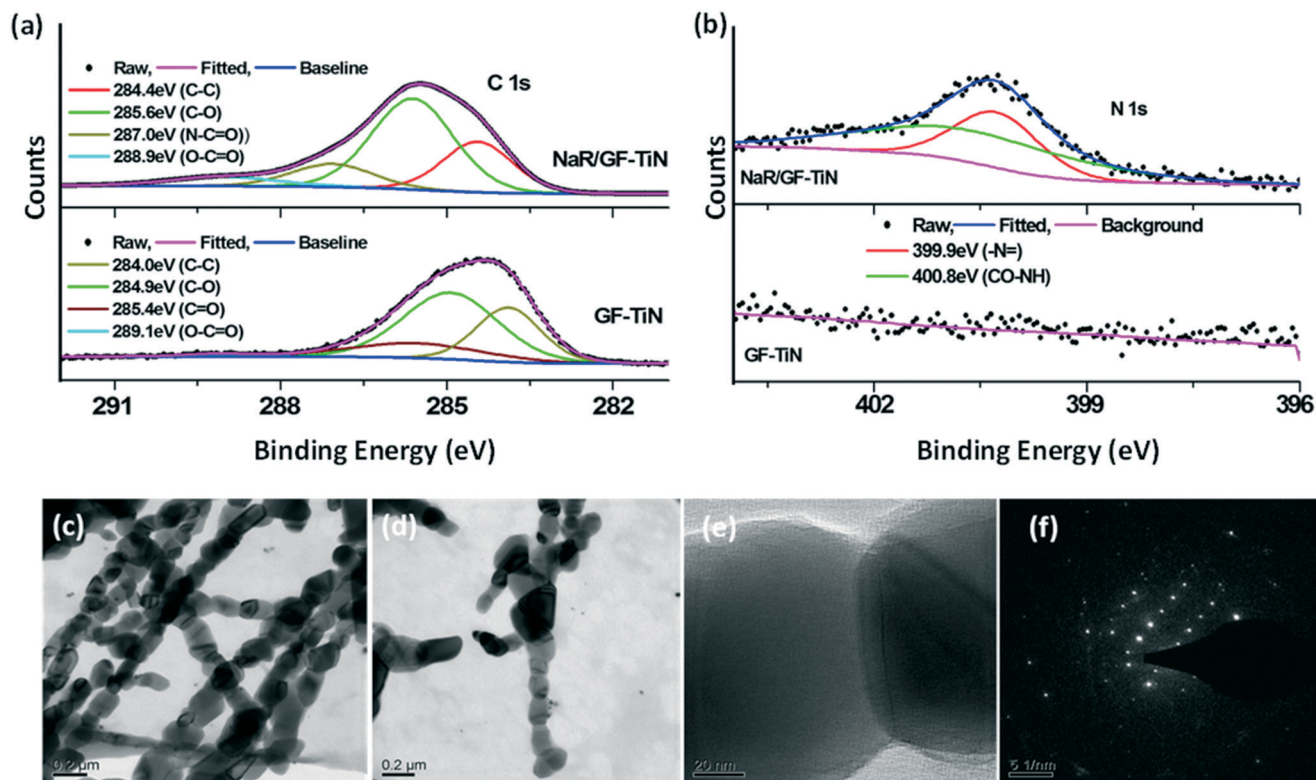
Fig. 4 (a and b) XPS spectra of C 1s (a) and N 1s (b) for mesoporous GF–TiN NF composites before and after the surface immobilization of NaR enzyme molecules. (c–e) TEM images for TiN NFs. (f) Electron diffraction pattern of TiN NFs.

scaffolds of NaR/GF–TiN NFs, which can lead to high stability and selectivity for the nitrate sensor.

Energy dispersive X-ray (EDX) spectroscopy (Fig. S7, ESI†) estimates the weight percentages of Ti (~90%), nitrogen (~8.07%), and residual carbon (1.87%). The residual carbon could prompt covalent interactions of TiN NFs with amide groups of the enzyme molecules. Table S1† summarizes the atomic percentages of each element (N, C, Ti and O) in the original TiO_2 and converted TiN NFs.

FESEM reveals the morphological transitions from the electrospun TiO_2 to TiN NFs. The electrospinning technique produces continuous TiO_2 NFs with no beads (Fig. S8a, ESI†). After the heat treatment under an ammonia atmosphere (see details in the materials and methods section), the obtained TiN NFs exhibit a truncated hexagonal shape of the nanocrystals that connected to each other to form bamboo-like continuous structures along the long axes of NFs (Fig. S8b–d, ESI†). Fig. 1d shows the GF scaffolds coated with the fragmented TiN NFs. The GF contains micro-sized pores and interconnected graphitic backbones, which allows TiN NFs to easily penetrate the interior of the GF and to be densely coated and packed on the scaffolds. Transmission electron microscopy (TEM) provides more detailed structural information on TiN NFs (Fig. 4c–e). Interestingly, the neighbouring hexagonal crystals of TiN share a common plane for site specific interconnections. The selected area electron diffraction (SAED) pattern (Fig. 4f) confirms the formation of various crystalline planes, (111),

(200), (220), (311) and (222), of TiN NFs, which agrees with the XRD results above.

Sensor characterization and validation

First, to investigate the electrochemical redox properties of the sensor, cyclic voltammetry (CV) studies are conducted on the sensor with and without TiN NFs functionalized on the GF scaffolds. The applied voltage potential ranges from −0.2 V to +0.8 V (Fig. 5a). The sensor using GO alone as the electrode (without TiN NFs) shows an electrochemical current of −14 µA at a potential of +0.2 V. The incorporation of TiN NFs into the GF improves the current to −75 µA, perhaps owing to improved redox reactivity and cycling performance, i.e., the discharge–charge rate,[42] of the composite electrode. The electrochemical current (I), diffusion coefficient (D), surface concentration (Γ), and heterogeneous electron transfer rate constant (k_s) of the GF and GF–TiN NF electrodes and NaR/GF–TiN NF bioelectrode for the ferro/ferricyanide redox couple are determined using eqn S1–S3 and summarized in Table S1 (ESI†). Compared to the GF electrode, the GF–TiN NF composite provides a higher diffusion coefficient for electrons generated from the ferro/ferricyanide redox reactions, due to the utilization of TiN NFs as electron conduction channels to facilitate the interfacial electron-transfer process across the electrode–electrolyte.[43] In the case of the enzyme incorporation into the GF–TiN NF composite, the diffusion coefficient of NaR/GF–TiN NFs further increases,
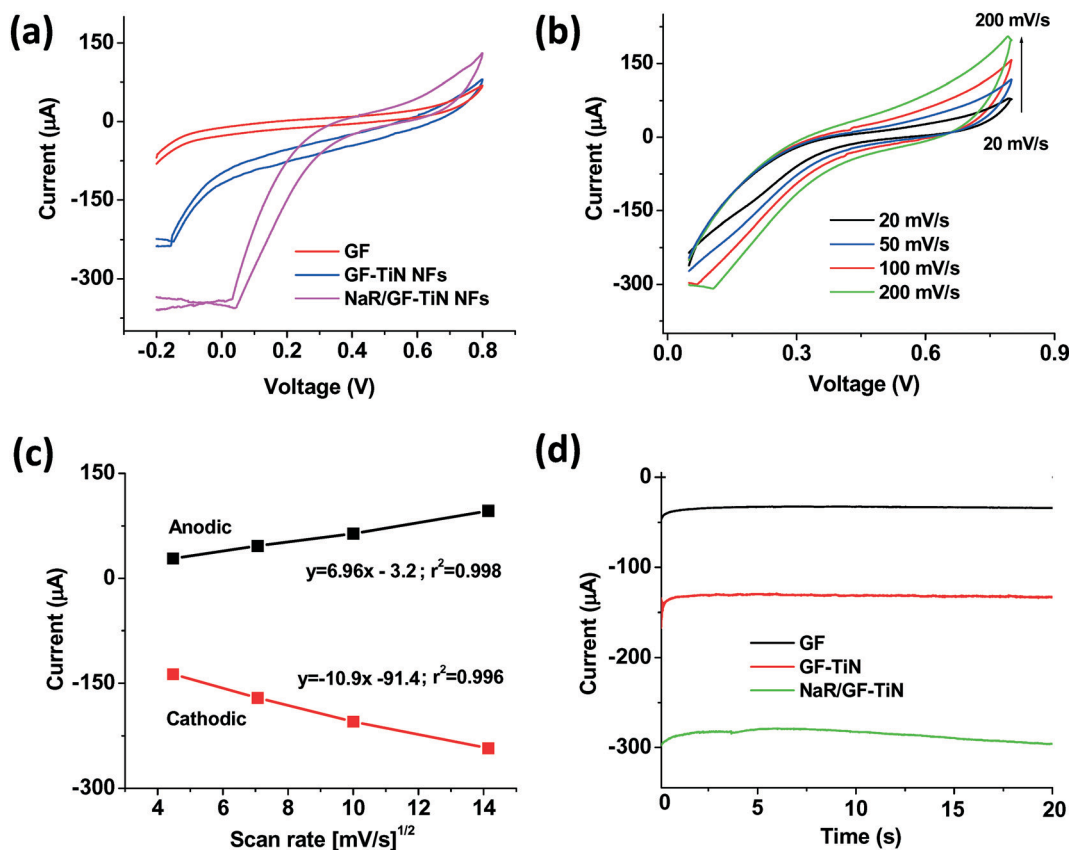
Fig. 5 (a) CV responses of the sensor using the GF and GF–TiN NF electrodes and NaR/GF–TiN NF bioelectrode at a scan rate of 50 mV s^{-1} in the presence of PBS (pH 7.4) containing an equimolar concentration (5 mM) of $[Fe(CN)_6]^{3-}$ and $[Fe(CN)_6]^{4-}$. (b) CV responses of the sensor with the NaR/GF–TiN NF bioelectrode as a function of scan rate (20–200 mV s^{-1}). (c) Anodic and cathodic currents *versus* the square root of the scan rates. (d) Chronoamperometry responses of the sensors using GF and GF–TiN NF electrodes and NaR/GF–TiN NF bioelectrode at a potential of −0.2 V.

perhaps because the NaR enzyme molecules in TiN NFs may appear in favorable orientations able to effectively activate the active sites at the enzyme to accelerate electrons generated from the redox reaction.[44,45] In addition, the NaR/GF–TiN NF bioelectrode gives maximum values of Γ = 72.8 × 10^{-9} mol cm^{-2} and k_s = 5.61 × 10^{-7} cm s^{-1}, compared to the GF and GF–TiN NF electrodes (Table S2†), suggesting that a larger number of redox moieties are available at the bioelectrode providing a higher faradic current.[46]

Fig. 5b shows the CV responses of the NaR/GF–TiN NF bioelectrode at a scan rate from 20 to 200 mV s^{-1}. With increasing scan rate, the peak-to-peak separation voltage for the NaR/GF–TiN NF bioelectrode shifts toward higher potentials. Because the anodic and cathodic peak currents are proportional and inversely proportional with the square root of the scan rates (Fig. 5c), respectively, the NaR/GF–TiN NF bioelectrode exhibits a surface-controlled process.[47]

Chronoamperometry is a widely used amperometric method to monitor the transient response of the working electrode of the electrochemical sensor with a potential pulse (*versus* the reference electrode). This method has a fast response and a high signal-to-noise ratio, compared to other amperometric techniques.[48] For the present sensor, the chronoamperometric current from the GF–TiN NF electrode

is found to be higher (−131 μA) than that from the GF electrode only (−33 μA), yielding a three-fold enhancement in current (Fig. 5d). After the immobilization of the NaR enzyme molecules, the output current of the sensor further increases to −292 μA.

With the excellent electrochemical performance of the NaR/GF–TiN NF bioelectrode demonstrated above, we further conduct chronoamperometric measurements for the sensor with synthetic test samples having nitrate concentrations ranging from 0.01 to 442 mg L^{-1} mixed in a PBS solution (see the sample preparation in the materials and methods section). Analyte solutions are injected through the inlet of the channel. Although the NaR/GF–TiN NF composite is embedded in the channel, the analytes can easily pass through the interior pores of the composite and exit at the outlet of the channel. The sensing potential is maintained at −0.2 V during the measurement, at which the immobilized NaR enzyme molecules dominate the specific reductive reaction at the electrode. Fig. 6a shows that the transient responses of the sensor exposed to different nitrate concentrations. The calibration curve of the sensor shown in Fig. 6b demonstrates that the chronoamperometric current increases almost proportional to the logarithm of nitrate concentration over the whole range of concentrations tested. The sensitivity of the
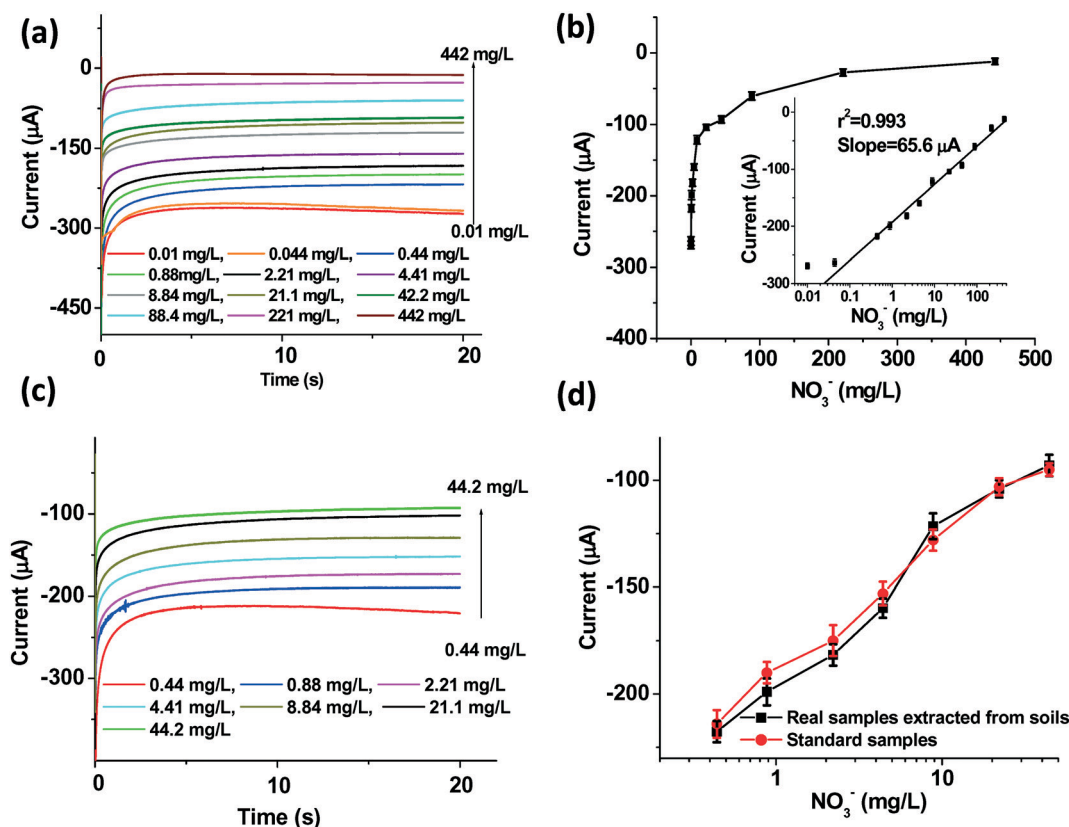
Fig. 6 (a) Chronoamperometric responses of the sensor with the NaR/GF–TiN NF bioelectrode as a function of nitrate concentration of the synthetic samples. (b) Sensor calibration plot showing the output current *versus* nitrate concentration. The inset shows the relationship between the logarithm of nitrate concentration and output current. (c) Chronoamperometric responses of the sensor to real samples extracted from soils. (d) Comparison plots for chronoamperometric signals of the sensor responding to synthetic and real soil samples. The error bars are obtained by calculating the standard deviation of three consecutive measurements for each concentration.

sensor is calculated to be 683.3 μA mg^{-1} L cm^{-2} based on the calibration curve. Using the NaR/GF–TiN NF bioelectrode, the sensor is capable of detecting minute concentrations of nitrate ions at 0.01 mg L^{-1}.

Next, we validate the sensor with the NaR/GF–TiN NF bioelectrode to detect nitrate concentrations of real solution samples extracted from the soil collected from a *Zea mays* farm field. The procedures for preparing the soil solution samples are described in the ESI.† In this measurement, −0.2 V is used as a sensing potential and the soil solutions are mixed with a PBS solution (pH = 7.4) containing [Fe(CN)$_6$]$^{3-/4-}$ and injected into the embedded channel. Fig. 6c presents the chronoamperometric currents of the sensor responding to different nitrate concentrations of soil solutions. As the concentration increases, the chronoamperometric current is found to increase due to the catalytic reduction of nitrate ions in the presence of NaR on the sensor surface (Fig. 6d). The average relative standard deviation (RSD) for the output current is less than ±4% for the real samples with nitrate concentrations of 2.21, 4.41, 8.84 and 22.1 mg L^{-1}; however, the value of RSD decreases to even only ±1% for 0.44, 0.88 and 44.2 mg L^{-1} concentrations (Fig. 6d). Therefore, this sensor demonstrates the considerable ability to quantify nitrate concentrations in the soil solution samples.

For the detection of nutrient ions in soil solutions, common measurement practices include using ion chromatography,[49] spectrophotometry,[50] ion-selective electrodes (ISEs),[51] and electrochemical sensors.[32–35] Among these practices, chromatography and spectrophotometry are limited to laboratories. The ISE-based and electrochemical sensors are field deployable and can convert the activity of a specific ion in a solution into an electrical signal.[23] Therefore, a number of chemically modified nitrate sensitive electrodes have been developed,[44,52] aiming at improving the performances of electrochemical nitrate sensors, such as sensitivity, dynamic range, LOD and selectivity. Table 1 compares the performances of our sensor with other reported electrochemical nitrate sensors. Our sensor provides a wide dynamic range of nitrate concentrations from 0.01 to 442 mg L^{-1}. The use of NaR/GF–TiN NF bioelectrode results in a significantly increased sensitivity (683.3 μA mg^{-1} L cm^{-2}) and decreased LOD (note: the lower the better) for the detection of nitrate, compared to the sensors using other nanostructured materials, such as reduced graphene oxide (GO),[33] 1-methyl-3-(pyrrol-1-ylmethyl)pyridinium,[34] wrinkled GO,[44] carbon nanotube–polypyrrole,[53] poly(3,4-ethylenedioxythiophene)-GO,[54] and Ag@iron oxide.[52] The improved performance of our sensor

Table 1 Performance comparison between our sensor and other typical existing nitrate sensors

Materials	Methods	Dynamic range $(mg\ L^{-1})$	Sensitivity $(\mu A\ mg^{-1}\ L\ cm^{-2})$	Limit of detection $(mg\ L^{-1})$	Ref.
Reduced GO	Amperometry	0.55–10.4	0.432	0.0625	33
1-Methyl-3-(pyrrol-1-ylmethyl)pyridinium	Amperometry	Up to 6.25	1.248	0.335	34
Copper	Linear sweep voltammograms	Up to 12.1	1.0987	NA	35
Methyl viologen/Nafion	Conductance	1.25–15.6	NA	0.312	36
Wrinkled GO	Cyclic voltammetry	0.0625–6.25	3.6	0.0625	44
Silver@iron oxide	Amperometry	Up to 62.5	10.6	1.8	52
Poly(3,4-ethylenedioxy-thiophene)-GO	Impedance	0.044–442	NA	0.135	54
CNT/polypyrrole	Amperometry	27.5–90.6	0.0048	10.6	55
Polypyrrole	Potentiometry	3.12–312.5	NA	0.625	56
Silver particle–polymethacrylic acid	Cyclic voltammetry	Up to 1250	2.08	31.2	57
GF–TiN NFs	Amperometry	0.01–442	683.3	0.01	This work
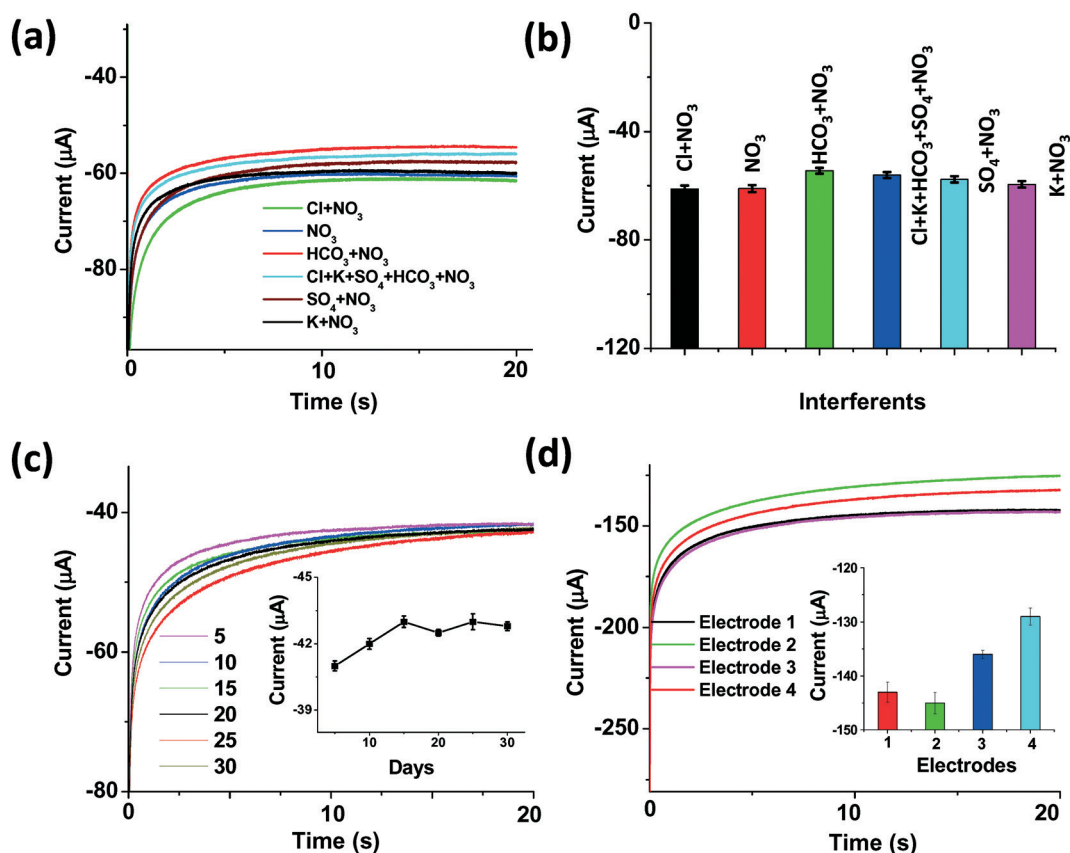
Fig. 7 (a) Chronoamperometric currents of the sensor responding to different interfering ions. The ion concentrations of Cl^-, K^+, HCO_3^-, and SO_4^{2-} are 12.7 mg L^{-1}, 5.12 mg L^{-1}, 1.63 mg L^{-1}, and 0.52 mg L^{-1}, respectively. These interfering ions are mixed with 442 mg L^{-1} nitrate ions. (b) Histogram plot showing the chronoamperometric currents of the sensor responding to different interfering ions. (c) Stability test conducted at a 5 day interval at a nitrate concentration of 442 mg L^{-1}. The inset shows the plot of current *versus* number of days. (d) Reproducibility test conducted at 8.84 mg L^{-1} nitrate concentration for four sensors. The inset shows the histogram plot for the current outputs of the sensors.

may be due to the enhanced electrochemical reactivity of the NaR/GF–TiN NF bioelectrode as it enables an improved loading capacity of enzyme molecules for catalytic reactions.

The effects of interfering ions for the GF–TiN NF based sensor are also investigated (Fig. 7a and b). A few types of interfering ions are included in the selectivity test, including

sulfate (SO_4^{2-}, 50 μM concentration), potassium (K^+, 200 μM), chloride (Cl^-, 450 μM), and bicarbonate (HCO_3^-, 100 μM). These ions are chosen because they are important anions and cations in agricultural soils. The concentration of nitrate ion is kept the same at 442 mg L^{-1} for all the cases. The measurements are conducted at a potential of −0.2 V (Fig. 7a). As shown in the chronoamperometric responses of the sensor to

these interfering ions (Fig. 7b), this sensor shows a good selectivity in the presence of the aforementioned interfering ions, as demonstrated by their RSD of ±2.4% from the initial values of the current. Because the immobilized NaR enzyme molecules on the surface of the GF–TiN composite restrict themselves from reducing oxo-compounds such as chloride, sulfate, and nitrite, the influences of different interfering ions are largely minimized for measuring complex real soil samples.

Furthermore, the stability of the sensor is evaluated at a 5 day interval over 30 days. The stability test involves exposing the sensor to the real soil solution sample (nitrate concentration: 8.84 mg L^{-1}) and, when not in use, storing the sensor at 4 °C. The results in Fig. 7c indicate that the sensor performance is considerably stable with a RSD value of ±2% from its initial response. In addition, for the reproducibility test (Fig. 7d), four identical sensors are prepared and chronoamperometric measurements are conducted with the same concentration of nitrate (44.2 mg L^{-1}). A RSD of ±5.3% from the initial current signal demonstrates a good reproducibility of the sensor for the detection of nitrate ions.

Conclusions

In summary, we have demonstrated the *in situ* integration of porous GF–TiN NF composites and microfluidic channels to realize high-performance microfluidic electrochemical sensors. The *in situ* assembly process utilizes the simple liquid-phase photopolymerization process, which enables convenient embedding of the GF-based electrochemical electrode into microfluidic channels or *vice versa*. As a result, the embedded GF–TiN NF based scaffolds allow analyte solutions to flow through and interact with the biomolecules covalently immobilized on the surface of the scaffolds. In addition, the unique combination of TiN NFs and GF produces synergy that results in the generation of a high-performance electrochemical electrode that provides improved electrochemical reactivity, heterogeneous electron transfer rate, and loading capacity of receptor biomolecules specific to target analytes. As an application demonstration, we have applied the GF–TiN NF nanocomposite and the *in situ* assembly technique together to form a microfluidic sensor for the detection of nitrate ions in soil solutions. The sensor utilizes NaR enzyme molecules to achieve high specificity to nitrate ions. The sensor provides a high sensitivity of 683.3 μA mg^{-1} L cm^{-2}, an extremely low LOD of 0.01 mg L^{-1}, and good reproducibility. This present sensor technology will be adopted for the detection of different ionic nutrients in soils such as phosphate, chloride and potassium ions, as well as other target biomolecules in many other applications, by functionalizing the GF–TiN NF-based electrodes with different specific molecules. It is believed that the present approach will lay a firm foundation to facilitate exploration of various GF-based microfluidic sensors for many emerging applications.

Notes and references

1 E. K. Sackmann, A. L. Fulton and D. J. Beebe, *Nature*, 2014, **507**, 181–189.
2 G. M. Whitesides, *Nature*, 2006, **442**, 368–373.
3 J. Kim, Z. Li and I. Park, *Lab Chip*, 2011, **11**, 1946–1951.
4 D. Vilela, J. Garoz, A. Colina, M. C. González and A. Escarpa, *Anal. Chem.*, 2012, **84**, 10838–10844.
5 P. Mostafalu, M. Akbari, K. A. Alberti, Q. Xu, A. Khademhosseini and S. R. Sonkusale, *Microfluid. Nanofluid.*, 2016, **2**, 16039.
6 Md A. Ali, P. R. Solanki, M. K. Patel, H. Dhayani, V. V. Agrawal, R. John and B. D. Malhotra, *Nanoscale*, 2013, **5**, 2883–2891.
7 Z. Chen, W. Ren, L. Gao, B. Liu, S. Pei and H. M. Cheng, *Nat. Mater.*, 2011, **10**, 424–428.
8 C. C. Kung, P. Y. Lin, F. J. Buse, Y. Xue, X. Yu, L. Dai and C. C. Liu, *Biosens. Bioelectron.*, 2014, **52**, 1–7.
9 Z. Niu, L. Liu, L. Zhang and X. Chen, *Small*, 2014, **10**, 3434–3441.
10 Y. He, W. Chen, X. Li, Z. Zhang, J. Fu, C. Zhao and E. Xie, *ACS Nano*, 2012, **7**, 174–182.
11 X. C. Dong, H. Xu, X. W. Wang, Y. X. Huang, M. B. Chan-Park, H. Zhang, L. H. Wang, W. Huang and P. Chen, *ACS Nano*, 2012, **6**, 3206–3213.
12 P. Si, X. C. Dong, P. Chen and D. H. Kim, *J. Mater. Chem. B*, 2013, **1**, 110–115.
13 X. Feng, Y. Zhang, J. Zhou, Y. Li, S. Chen, L. Zhang, Y. Ma, L. Wang and X. Yan, *Nanoscale*, 2015, **7**, 2427–2432.
14 Y. Ma, M. Zhao, B. Cai, W. Wang, Z. Ye and J. Huang, *Biosens. Bioelectron.*, 2014, **59**, 384–388.
15 Md. A. Ali, K. Mondal, Y. Jiao, S. Oren, Z. Xu, A. Sharma and L. Dong, *ACS Appl. Mater. Interfaces*, 2016, **8**, 20570–20582.
16 J. Zhi, W. Zhao, X. Liu, A. Chen, Z. Liu and F. Huang, *Adv. Funct. Mater.*, 2014, **24**, 2013–2019.
17 M. Yuan, A. Liu, M. Zhao, W. Dong, T. Zhao, J. Wang and W. Tang, *Sens. Actuators, B*, 2014, **190**, 707–714.
18 Y. Xue, D. Yu, L. Dai, R. Wang, D. Li, A. Roy, F. Lu, H. Chen, Y. Liu and J. Qu, *Phys. Chem. Chem. Phys.*, 2013, **15**, 12220–12226.
19 T. Zhang, W. Wang, D. Zhang, X. Zhang, Y. Ma, Y. Zhou and L. Qi, *Adv. Funct. Mater.*, 2010, **20**, 1152–1160.

20 Md A. Ali, K. Mondal, C. Singh, B. D. Malhotra and A. Sharma, *Nanoscale*, 2015, **7**, 7234–7245.

21 D. Li and Y. Xia, *Nano Lett.*, 2003, **3**, 555–560.

22 Z. Li, H. Zhang, W. Zheng, W. Wang, H. Huang, C. Wang, A. G. MacDiarmid and Y. Wei, *J. Am. Chem. Soc.*, 2008, **130**, 5036–5037.

23 K. Mondal, Md A. Ali, V. V. Agrawal, B. D. Malhotra and A. Sharma, *ACS Appl. Mater. Interfaces*, 2014, **6**, 2516–2527.

24 W. Li, C.-Y. Cao, C.-Q. Chen, Y. Zhao, W.-G. Song and L. Jiang, *Chem. Commun.*, 2011, **47**, 3619–3621.

25 J. H. Bang and K. S. Suslick, *Adv. Mater.*, 2009, **21**, 3186–3190.

26 H. Li, W. Pan, W. Zhang, S. Huang and H. Wu, *Adv. Funct. Mater.*, 2013, **23**, 209–214.

27 Y. Dong, Y. Wu, M. Liu and J. Li, *ChemSusChem*, 2013, **6**, 2016–2021.

28 Y. Qiu, K. Yan, S. Yang, L. Jin, H. Deng and W. Li, *ACS Nano*, 2010, **4**, 6515–6526.

29 D. J. Beebe, J. S. Moore, Q. Yu, R. H. Liu, M. L. Kraft, B. H. Jo and C. Devadoss, *Proc. Natl. Acad. Sci. U. S. A.*, 2000, **97**, 13488–13493.

30 L. Dong, A. K. Agarwal, D. J. Beebe and H. Jiang, *Nature*, 2006, **442**, 551–554.

31 R. W. Jones, S. J. Rathke, D. A. Laird and J. F. McClelland, *Appl. Spectrosc.*, 2013, **67**, 1106–1110.

32 S. Cosnier, C. Innocent and Y. Jouanneau, *Anal. Chem.*, 1994, **66**, 3198–3201.

33 V. Mani, A. P. Periasamy and S.-M. Chen, *Electrochem. Commun.*, 2012, **17**, 75–78.

34 L. M. Moretto, P. Ugo, M. Zanata, P. Guerriero and C. R. Martin, *Anal. Chem.*, 1998, **70**, 2163–2166.

35 Y. Li, Y. H. Li, H. Y. Song, H. Lu, J. Sun, J. Tong, C. Bian and S. Xia, *SENSORS, 2015 IEEE*, 2015, 1–4.

36 X. J. Wang, S. V. Dzyadevych, J. M. Chovelon, N. J. Renault, L. Chen, S. Q. Xia and J. F. Zhao, *Electrochem. Commun.*, 2006, **8**, 201–205.

37 A. A. Gokhale, J. Lu, R. R. Weerasiri, J. Yu and I. Lee, *Electroanalysis*, 2015, **27**, 1127–1137.

38 H. Jiang, L. J. Halverson and L. Dong, *J. Micromech. Microeng.*, 2015, **25**, 125017.

39 J. Moorthy and D. J. Beebe, *Lab Chip*, 2003, **3**, 62–66.

40 P. LeClair, G. P. Berera and J. S. Moodera, *Thin Solid Films*, 2000, **376**, 9–15.

41 C. P. Constable, J. Yarwood and W. D. Munz, *Surf. Coat. Technol.*, 1999, **116**, 155–159.

42 G. Hu, C. Xu, Z. Sun, S. Wang, H. M. Cheng, F. Li and W. Ren, *Adv. Mater.*, 2015, **28**, 1603–1609.

43 A. S. Ghrera, C. M. Pandey, Md A. Ali and B. D. Malhotra, *Appl. Phys. Lett.*, 2015, **106**, 193703.

44 Md A. Ali, W. Hong, S. Oren, Q. Wang, Y. Wang, H. Jiang and L. Dong, *RSC Adv.*, 2016, **6**, 67184–67195.

45 R. Sharma, Md A. Ali, N. R. Selvi, V. N. Singh, R. K. Sinha and V. V. Agrawal, *J. Phys. Chem. C*, 2014, **118**, 6261–6271.

46 S. Park, K. Cho and S. Kim, *Trans. Electr. Electron. Mater.*, 2014, **15**, 136–138.

47 M. Thompson, G. G. Wildgoose and R. G. Compton, *ChemPhysChem*, 2006, **7**, 1328–1336.

48 Md A. Ali, S. Srivastava, P. R. Solanki, V. Reddy, V. V. Agrawal, C. Kim, R. John and B. D. Malhotra, *Sci. Rep.*, 2013, **3**(2661), 1–9.

49 K. Ito, Y. Takayama, N. Makabe, R. Mitsui and T. Hirokawa, *J. Chromatogr. A*, 2005, **1083**, 63–67.

50 K. M. Miranda, M. G. Espey and D. A. Wink, *Nitric Oxide*, 2001, **5**, 62–71.

51 J. E. Davies, G. J. Moody and J. D. Thomas, *Analyst*, 1972, **97**, 87–94.

52 M. Bonyani, A. Mirzaei, S. G. Leonardi, A. Bonavita and G. Neri, *Electroanalysis*, 2015, **27**, 2654–2662.

53 F. Can, S. K. Ozoner, P. Ergenekon and E. Erhan, *Mater. Sci. Eng., C*, 2012, **32**, 18–23.

54 Md. A. Ali, H. Jiang, N. K. Mahal, R. J. Weber, R. Kumar, M. J. Castellano and L. Dong, *Sens. Actuators, B*, 2017, **239**, 1289–1299.

55 F. Can, S. K. Ozoner, P. Ergenekon and E. Erhan, *Mater. Sci. Eng., C*, 2012, **32**, 18–23.

56 M. Sohail and S. B. Adeloju, *Electroanalysis*, 2009, **21**, 1411–1418.

57 S. G. Leonardi, N. Donato, A. Bonavita, G. Neri, M. Bonyani and A. Mirzaei, *AISEM Annual Conference, IEEE, XVIII*, 2015, 1–4, DOI: 10.1109/AISEM.2015.7066829.